LETTER

https://doi.org/10.1038/s41586-019-1078-6

Five decades of northern land carbon uptake revealed by the interhemispheric CO_2 gradient

P. Ciais[1,2]*, J. Tan[2], X. Wang[2], C. Roedenbeck[3], F. Chevallier[1], S.-L. Piao[2,4], R. Moriarty[5], G. Broquet[1], C. Le Quéré[5], J. G. Canadell[6], S. Peng[2], B. Poulter[7], Z. Liu[5,8,9] & P. Tans[10]

The global land and ocean carbon sinks have increased proportionally with increasing carbon dioxide emissions during the past decades[1]. It is thought that Northern Hemisphere lands make a dominant contribution to the global land carbon sink[2–7]; however, the long-term trend of the northern land sink remains uncertain. Here, using measurements of the interhemispheric gradient of atmospheric carbon dioxide from 1958 to 2016, we show that the northern land sink remained stable between the 1960s and the late 1980s, then increased by 0.5 ± 0.4 petagrams of carbon per year during the 1990s and by 0.6 ± 0.5 petagrams of carbon per year during the 2000s. The increase of the northern land sink in the 1990s accounts for 65% of the increase in the global land carbon flux during that period. The subsequent increase in the 2000s is larger than the increase in the global land carbon flux, suggesting a coincident decrease of carbon uptake in the Southern Hemisphere. Comparison of our findings with the simulations of an ensemble of terrestrial carbon models[5,8] over the same period suggests that the decadal change in the northern land sink between the 1960s and the 1990s can be explained by a combination of increasing concentrations of atmospheric carbon dioxide, climate variability and changes in land cover. However, the increase during the 2000s is underestimated by all models, which suggests the need for improved consideration of changes in drivers such as nitrogen deposition, diffuse light and land-use change. Overall, our findings underscore the importance of Northern Hemispheric land as a carbon sink.

Carbon dioxide emissions from fossil-fuel consumption and cement production, and land use change increased by a factor of three between 1960 and 2016. The growth rate of emissions was fast in the 1980s, slower in the 1990s and then re-accelerated[9] in the 2000s. The global land and ocean carbon sinks increased proportionally with growing emissions[1]; however, their location and trends are not completely understood. Northern Hemisphere lands make a dominant contribution to the global land carbon sink[2–7]. In the Northern Hemisphere mid- and high latitudes, vegetation greenness has increased in the past 30 years[10] and the seasonal amplitude of CO_2 has increased by 50% in the past 50 years[11], which suggests an increase in the fixation of CO_2 by photosynthesis. However, these observations are not proof that the Northern Hemisphere net carbon sink is increasing, because of possible upward trends in respiration[12] and land-use emissions compensating for increased uptake by photosynthesis.

To gain insights into the long-term trend in the northern land sink over the past 50 years, we use the interhemispheric gradient of atmospheric CO_2, which is defined as the observed difference in atmospheric CO_2 between the Mauna Loa station (located at 19° N) and the South Pole. Both the Mauna Loa and the South Pole stations record CO_2 growth rates that are representative of the means in their respective hemispheres[13]. Here we examine the relationship between the interhemispheric gradient (IG) and fossil-fuel and cement CO_2 emissions (F) between 1958 and 2016. We also look at recent changes during the 2000s—a period marked by the acceleration of global CO_2 emissions, arising mainly from east and south Asia[8,14].

From 1958 to 2016 the interhemispheric gradient grew in proportion to emissions from fossil fuels and cement (Fig. 1, Extended Data Fig. 1) with a Pearson correlation coefficient (r) of 0.97 ($P < 0.01$) and a mean regression slope[15] of 0.44 ± 0.01 p.p.m. per Pg C per year (Methods). This close linear relationship is an emergent property of the carbon cycle perturbed by human activities[16]. It suggests that the difference in carbon sinks between the Northern and Southern hemispheres has increased and has kept pace with the upward trend in emissions from fossil fuels and cement (Methods, Extended Data Fig. 1). Between the 1960s and the decade 2007–2016, the increase in fossil-fuel and cement emissions alone would suggest an increase in the interhemispheric gradient of 4.4 ± 0.2 p.p.m. (Methods); however, observations show that the increase was only 3.9 ± 0.08 p.p.m. As such, even if the relationship shown in Fig. 1 is dominated by the increase in fossil-fuel and cement emissions, this cannot be the full explanation. The increasing difference between the Northern and Southern Hemisphere carbon sinks that is suggested in Fig. 1 could reflect trends in either hemisphere. A persistent reduction of the Southern Ocean uptake over 50 years as the sole explanation for the IG–F relationship shown in Fig. 1 is implausible. This would require a sustained decrease of the Southern Ocean sink at a mean rate of 0.6 Pg C yr^{-1} per decade, which is inconsistent with findings that show a small weakening[17] during 1981–2002 and a strengthening thereafter[18]. A declining sink or an increasing source in southern terrestrial ecosystems is also unlikely: because most Southern Hemisphere forests are close to the equator, a trend in their CO_2 balance has only a weak effect on the interhemispheric gradient. In addition, declining carbon accumulation in tropical-forest biomass over the Amazon (shown for the past two decades in ref. [19], and here extrapolated to the past five decades) or increasing emissions from Southern Hemisphere land-use change[20] are too small to explain the data presented in Fig. 1. The most plausible hypothesis is that an increasing trend in the Northern Hemisphere land and ocean fluxes explains the observed trends in the interhemispheric gradient.

Superimposed on the long-term linear trend, there is decadal variability of the interhemispheric gradient relative to emissions. Relative to the linear fit defined by all years (Fig. 1), values of the interhemispheric gradient were above the line in the late 1990s, fell below it during the 2000s ($P < 0.01$), and then returned close to the line again after 2010. The IG–F linear regression slope calculated using data recorded at the Mauna Loa station decreased by 0.5 p.p.m. per Pg C per year between the period spanning the early 1980s to 1999 (period 1) and the following period from 2000 to 2009 (period 2). The IG–F linear regression slopes calculated using data obtained from seven long-term Northern Hemisphere atmospheric CO_2 stations with at least 20 years of measurements (Methods) exhibit decadal changes that are consistent with those

[1]Laboratoire des Sciences du Climat et de l'Environnement, IPSL-LSCE, CEA-CNRS-UVSQ-UPSACLAY, Gif sur Yvette, France. [2]Sino-French Institute for Earth System Science, College of Urban and Environmental Sciences, Peking University, Beijing, China. [3]Max Planck Institut für Biogeochemie, Jena, Germany. [4]Institute of Tibetan Plateau Research, Chinese Academy of Sciences, Beijing, China. [5]Tyndall Centre for Climate Change Research, School of Environmental Sciences, University of East Anglia, Norwich, UK. [6]CSIRO Oceans and Atmosphere, Canberra, Australian Capital Territory, Australia. [7]NASA Goddard Space Flight Center, Biospheric Sciences Lab, Greenbelt, MD, USA. [8]Department of Earth System Science, Tsinghua University, Beijing, China. [9]The Environment and Natural Resources Program, John F. Kennedy School, Harvard University, Cambridge, MA, USA. [10]NOAA Earth System Research Laboratory, Boulder, CO, USA. *e-mail: philippe.ciais@lsce.ipsl.fr

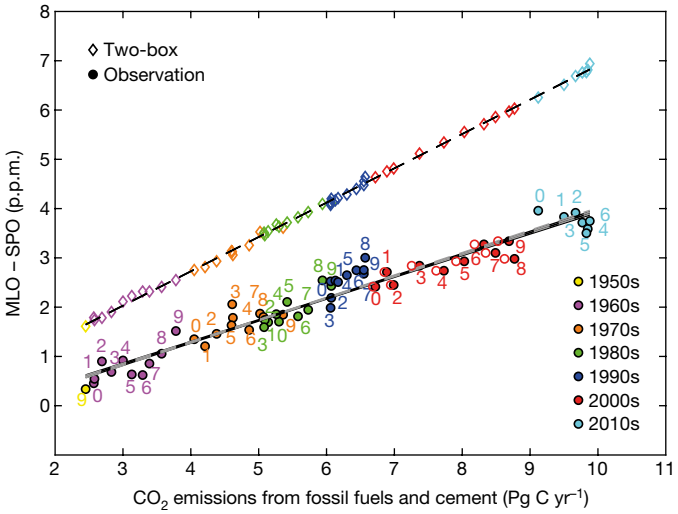

Fig. 1 | Relationship between the interhemispheric gradient of CO_2 and fossil-fuel and cement CO_2 emissions. The solid line is an orthogonal data regression fit to all years of data. The numbers next to each point are the specific years of the record within the decade indicated by the colour code. The empty circles (for the 2000s) are the results using, for China, emission values from ref. [14] (which are lower than other estimates), and for all other countries and international fuels, the emission values from the Carbon Dioxide Information Analysis Center (CDIAC; ref. [9]). The dashed line and diamonds show the increase of the gradient predicted from a two-box atmospheric model, based on the increase of fossil-fuel emissions alone.

observed at Mauna Loa (Extended Data Fig. 2). A plot of the values of the IG–F slopes from these seven stations shows that the slopes decrease between periods 1 and 2 (Fig. 2, Extended Data Tables 1, 2). Below we examine possible explanations for the decreased sensitivity of the interhemispheric gradient to emissions from fossil fuels and cement that is seen during the 2000s.

In the 1960s, the largest fraction (75%) of global fossil-fuel and cement emissions was from Europe and North America. In the 2000s, these two regions accounted for only 45% of such emissions; the rest were from Asia. In the past two decades, fossil-fuel and cement emissions have increased predominantly in east and south Asia; that is, closer to the western Pacific intertropical convergence zone and the Asian monsoon convergence zone (Extended Data Fig. 3), where CO_2 emitted at the surface is uplifted by convection and transported across the equator towards the Southern Hemisphere[21]. The southward and eastward shift of these emissions leads us to expect a decrease of the IG–F slope in the 2000s at northern mid-latitude stations in North America and Europe, paralleled with an increase at stations located in the western Pacific and close to east Asia.

We simulated the distribution of a fossil-fuel CO_2 tracer with two different transport models, LMDZ (ref. [22]) and TM3 (ref. [23]), between 1979 and 2013. Both models were prescribed with interannual wind fields (two different fields for TM3) and geographically variable emissions (Methods). These simulations revealed a strong linear relationship between $IG^{\text{fossil tracer}}_{\text{modelled}}$ and fossil-fuel and cement emissions at all northern stations, where $IG^{\text{fossil tracer}}_{\text{modelled}}$ is the modelled interhemispheric gradient of the fossil-fuel CO_2 tracer. The two TM3 simulations showed only a small decrease in the simulated $IG^{\text{fossil tracer}}_{\text{modelled}}$ – F slopes (Extended Data Fig. 3) during the 2000s compared to the previous decades—well below the observed decrease of the IG–F slope— and the LMDZ simulation showed almost no change in the slope. From this, we conclude that the increase of fossil-fuel and cement emissions in Asian regions closer to the intertropical convergence zone accounted for less than 5% of the observed decrease of IG–F slopes in the 2000s. This small contribution is further supported by the fact that, during 2010–2014, the interhemispheric gradient returned to values close to those defined by the long-term mean IG–F regression (Fig. 1), while emissions from Asia remained high.

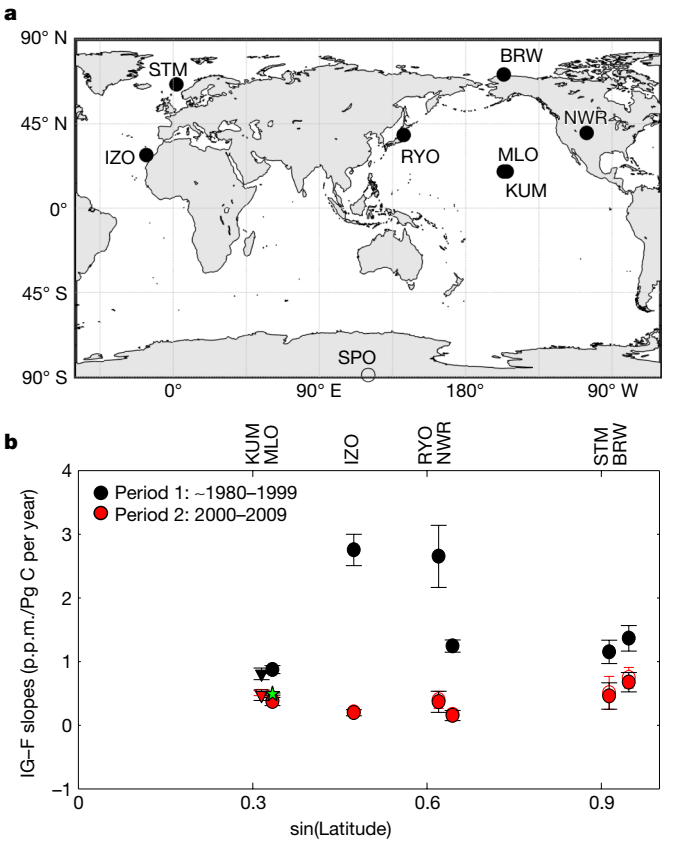

Fig. 2 | Slopes of linear regression fits between interhemispheric gradient and fossil-fuel emissions, using data from long-term Northern Hemisphere atmospheric stations. a, Map of selected stations (see Methods). BRW, Point Barrow, Alaska, National Oceanic and Atmospheric Administration Earth System Research Laboratory (NOAA ESRL); STM, Station M (NOAA ESRL); NWR, Niwot Ridge, Colorado (NOAA ESRL); RYO, Ryori, Japan (Japan Meteorological Agency, JMA); IZO, Izana, Tenerife Islands (Izana Observatory-Meteorological State Agency of Spain IO-MSAS); KUM, Cape Kumukahi, Hawaii (NOAA ESRL); MLO, Mauna Loa, Hawaii (Scripps); and SPO, South Pole (Scripps). **b**, Values of IG–F slopes measured at each station for periods 1 and 2. The black circles are the values of the slopes during the first period (around 1980–1999) and the red circles are the values during the second period (2000–2009), with error bars from orthogonal data regression[15]. Out of 11 stations, only the seven with absolute correlation coefficient values of greater than 0.3 are shown (Extended Data Table 1). The green star is the long-term mean slope over 1958–2016 from Mauna Loa. Filled symbols represent fossil-fuel CO_2 emissions obtained from CDIAC, whereas open symbols (for the 2000s; overlaid with filled symbols) are obtained using fossil CO_2 emissions from ref. [14] for China and from CDIAC for all other countries.

A second mechanism that can explain the values that fall beneath the linear fit of the interhemispheric gradient relative to fossil-fuel and cement emissions in the 2000s is an increase in the difference between the Northern and Southern Hemisphere sinks. We applied a two-box inversion model to diagnose changes in the Northern Hemisphere land sink (L_N) from observations of the interhemispheric gradient and of the CO_2 growth rate over the past five decades. The northern land sink is given by:

$$L_N = \frac{1}{2}\left[(F_N - F_S) + L - (O_N - O_S) - 2\alpha\tau^{-1}\mathrm{IG}\right] \quad (1)$$

The sign convention is positive for F (which represents emission from fossil fuels and cement) and negative for sinks, and we used $-L$ and $-O$ for land and ocean sinks, respectively, to present positive values for sinks. A very small term containing the difference in growth rates

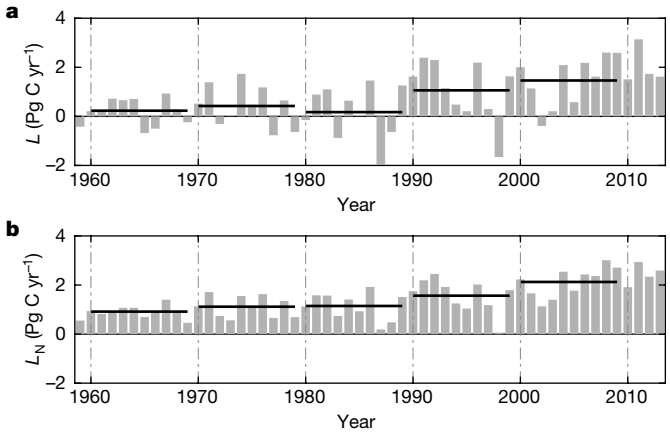

Fig. 3 | Global and Northern Hemisphere land fluxes. a, Global net land flux (L), this flux includes land-use change emissions and other processes causing land uptake. **b**, Northern land sink (L_N) inferred from the two-box inversion model constrained by measurements of the interhemispheric gradient and the ocean sink interhemispheric difference from ocean models (Methods).

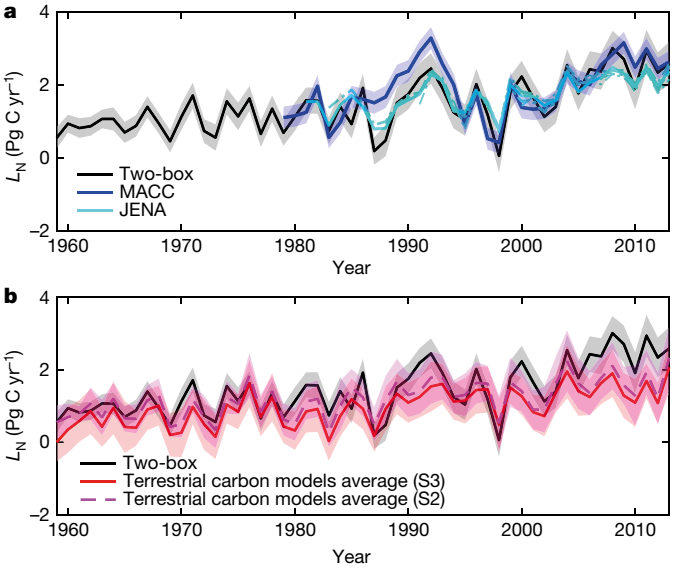

Fig. 4 | Variations in the northern land sink during the past 56 years. a, The northern land sink obtained from the two-box inversion, the MACC and the JENA 3D inversions. Shaded areas are 1-sigma uncertainties for the two-box inversion (Methods) and for MACC. The different cyan lines represent different atmospheric networks used by the JENA inversion. **b**, L_N^{models} from nine land carbon-cycle models driven by climate, increasing CO_2 levels and land cover change (S3 simulation in red; shaded areas represent the standard deviation of the models). Results from simulation S2 without land-use change are shown by a dashed pink line.

in both hemispheres is not reported in equation (1) for simplicity, but was included in the two-box inversion (see Methods). L is the global net land flux including land-use emissions, and is deduced from the global CO_2 budget equation; $O_N - O_S$ is the ocean sink interhemispheric difference; α is a conversion factor[24]; and τ is the interhemispheric CO_2 mixing time, which is set to 1.4 years[25]. For annual $O_N - O_S$ values, we used the mean value from seven ocean models driven by increasing CO_2 and variable climate[8] during the past 50 years (uncertainty from their 1-sigma standard deviation; Extended Data Fig. 4).

We found that L_N is an average sink of 1.4 ± 0.4 Pg C yr^{-1} between 1959 and 2013, and is a sink in each individual year. L_N shows an average positive trend of 0.3 ± 0.2 Pg C yr^{-1} per decade (Mann–Kendall test; $P < 0.05$), which is nearly identical to the positive trend of L. The fact that L_N increased at the same rate as L suggests that the Southern Hemisphere land flux remained stable over this time. Figure 3 shows a net increase of L between 1989 and 1994, followed by a period of oscillations until a continuously large land sink prevailed after the mid-2000s. Coincident with this increase of L was an increasing trend of L_N ($P < 0.05$) (Fig. 3). Between the period 1960–1990 and the 1990s, L_N increased by 0.5 ± 0.4 Pg C yr^{-1} and L increased by 0.9 Pg C yr^{-1}. The increase of L_N in the 1990s thus accounted for 65% of the global increase in L (Extended Data Table 3). Between the 1990s and the 2000s, L_N increased by 0.6 ± 0.5 Pg C yr^{-1} and L increased by only 0.4 ± 0.6 Pg C yr^{-1} (Extended Data Table 3), a result which implies either a weaker land carbon uptake in the Southern Hemisphere by 0.2 Pg C yr^{-1}—which is roughly consistent with available forest inventories data[7,19]—or a weaker southern ocean sink, which is not confirmed by ocean models[8] or data-driven modelled estimates[26,27]. Similar results were also found when values of $O_N - O_S$ after the mid-1980s were obtained from data-driven models[26,27] instead of from ocean models (Extended Data Fig. 4).

Emissions from fossil fuels and cement grew by 0.9 Pg C yr^{-1} between the 1980s and the 1990s, and by 1.5 Pg C yr^{-1} between the 1990s and the 2000s. Despite this increased forcing of the carbon cycle, the L_N/F ratio does not show substantial change between any of the past five decades, ranging from a minimum of 0.21 in the 1980s to a maximum of 0.27 in the 2000s. Arguably, the two-box inversion of L_N has systematic uncertainties that can be attributed to assumptions that the Mauna Loa and South Pole measurements represent hemispheric-mean CO_2 concentrations, to the aggregation of atmospheric transport and to surface fluxes. For the period between 1979 and 2013, we compared the values of L_N obtained from two-box inversion with the results of two other inversions[28,29]—MACC and JENA (CarboScope)—which are based on three-dimensional (3D) transport models solving for weekly fluxes in each grid cell of the globe and using CO_2 records from more than 100 stations (Methods). Within their relative uncertainties, JENA and the two-box inversion model yield L_N values that are consistent with each other ($R = 0.92$). MACC and the two-box inversion model show consistent L_N variations ($R = 0.77$; Extended Data Fig. 5), but the decadal L_N value obtained by MACC is higher than that obtained from two-box inversion for the late 1980s and early 1990s (Fig. 4). Overall this suggests that the two-box inversion model, despite its simplicity, accounts for both the mean value of and the variations in L_N.

In the two-box inversion model, the interhemispheric atmospheric mixing time τ was fixed at 1.4 ± 0.2 years[21]. One difficulty in assessing possible temporal variations of τ is that it depends on the air mass exchange convoluted with spatiotemporal emission patterns of each tracer, which the two-box model cannot resolve. Sulfur hexafluoride (SF_6)—a tracer that is emitted only by anthropogenic activities and is measured at long-term stations (http://agage.mit.edu)—can be used as a proxy of fossil-fuel CO_2 to provide insights into possible changes of τ[4,25]. During the period 1996–2008, changes in the interhemispheric gradient of SF_6 were explained predominantly (60%) by a southward displacement of SF_6 emissions, and to a lesser extent (40%) by a decreasing interhemispheric mixing time (τ_{SF6}), according to ref. [25]. We constructed an extreme scenario for the two-box inversion, assuming that τ_{CO2} decreased linearly at the same rate as τ_{SF6} during the entire period from 1990 to 2010. This scenario produces a smaller increase in L_N compared to if τ was constant, and gave an increase in L_N of 0.4 ± 0.5 Pg C yr^{-1} between the 1990s and the 2000s; that is, 73% of the increase obtained with constant τ (Extended Data Fig. 5). From this, we conclude that up to 30% of the magnitude of the decadal shift of L_N in the 2000s might be explained by a decreasing τ. More complex trends in atmospheric transport—which are not modelled in the two-box inversion—could also bias the inferred L_N, in particular trends in the so-called atmospheric transport rectifier effect[30]. We used the TM3 transport model to address this question, and verified that 'rectifier trends'—which are related to the co-variation between trends in seasonal transport and trends in de-seasonalized land fluxes—did not produce any trend in interhemispheric gradient, and therefore are not a source of systematic error in the two-box inference of L_N (Extended Data Fig. 6).

Finally, we compared the time series of L_N in Fig. 3 with the simulations of terrestrial carbon models over the same period (Extended Data Table 3, Extended Data Fig. 7). We used the results from nine models[5,8] (TRENDY-V4) that include land cover change, fire, climate change and CO_2 fertilization effects. Three of these models represent carbon–nitrogen interactions, which can either limit or enhance carbon sinks—the latter over temperate regions where most nitrogen deposition occurs. The mean of terrestrial carbon models gives a northern land sink L_N^{models} that is, on average, lower than L_N from the two-box inversion model for all decades (Fig. 4, Extended Data Table 1). For the simulations without land-use change (Fig. 4) the obtained values of L_N^{models} are slightly larger—because land use in the Northern Hemisphere was dominated by agricultural abandonment, which causes carbon sequestration—however, they were still below the values obtained from the two-box inversion. The mean L_N^{models} has a higher temporal year-to-year correlation ($R = 0.79$) with measured values of L_N than with those from any individual model. Between the 1980s and the 1990s, all models predict an increase of L_N^{models} of the same magnitude as that observed in the two-box inversion (0.5 ± 0.4 Pg C yr^{-1}). Between the 1990s and 2000s, however, the models do not reproduce the observation-based increase of L_N obtained by the two-box inversion (Extended Data Table 3).

The three models that represent carbon–nitrogen interactions and are driven by variable nitrogen deposition simulate, in the 2000s, an increase of L_N^{models} (up to 0.2 Pg C yr^{-1}) that is at the lower end of the observed increase from inversions (0.2 to 0.6 Pg C yr^{-1}). By contrast, two of the six models without carbon–nitrogen interactions did not reproduce any increase of L_N^{models} (Extended Data Fig. 7, Extended Data Table 3). No conclusion can be drawn from a sample of three models about the role of increased nitrogen deposition, and the difference in the increase in L_N^{models} between carbon–nitrogen models and carbon-only models is not significant.

More than two decades ago, two notable studies were published in the field: one inferred a large northern land sink[2], whereas another[3] explained most of the northern sink by ocean uptake. Since then, multiple streams of evidence have confirmed the existence of a persistent land carbon sink. The long-term average value of this sink that we infer here—using the longest atmospheric CO_2 records—is higher than that obtained from the results of terrestrial carbon-cycle models. Terrestrial models capture the interannual variability of L_N well, but they underestimate the recent increase of L_N in the 2000s. It is likely that they underestimate the recent effect of increased nitrogen deposition[31] over Chinese and Siberian forests, given that the fertilizing effects of nitrogen on forest growth are larger at low exposure levels[32]. Additional drivers that were not included in the models are increasing diffuse light fraction from aerosol-scattering effects, in particular over east Asia[33], as well as expanding young forests and plantations in this region. This study underscores the need for a coordinated stewardship of the northern land sink as part of the climate policy agenda, with the objective to maintain land sinks through favourable land use and enhance them whenever possible. It also highlights the need for enhanced observations, particularly over regions that are poorly covered by observations at present—such as Eastern Europe, Siberia and the Arctic. It is from these far northern regions that positive and negative carbon–climate feedbacks are most likely to arise in the future.

Online content

Any methods, additional references, Nature Research reporting summaries, source data, statements of data availability and associated accession codes are available at https://doi.org/10.1038/s41586-019-1078-6.

Received: 26 November 2016; Accepted: 25 January 2019;
Published online 3 April 2019.

1. Ballantyne, A. P., Alden, C. B., Miller, J. B., Tans, P. P. & White, J. W. C. Increase in observed net carbon dioxide uptake by land and oceans during the past 50 years. *Nature* **488**, 70–72 (2012).
2. Tans, P. P., Fung, I. Y. & Takahashi, T. Observational constraints on the global atmospheric CO_2 budget. *Science* **247**, 1431–1438 (1990).
3. Keeling, C. D., Piper, S. C. & Heimann, M. *Aspects of Climate Variability in the Pacific and the Western Americas* Vol. 55 (ed. Peterson, D. H.) 305–363 (AGU, 1989).
4. Wang, Y., Li, M. & Shen, L. Accelerating carbon uptake in the Northern Hemisphere: evidence from the interhemispheric difference of atmospheric CO_2 concentrations. *Tellus B* **65**, 20334 (2013).
5. Sitch, S. et al. Recent trends and drivers of regional sources and sinks of carbon dioxide. *Biogeosciences* **12**, 653–679 (2015).
6. Ciais, P. et al. Can we reconcile atmospheric estimates of the Northern terrestrial carbon sink with land-based accounting? *Curr. Opin. Environ. Sustain.* **2**, 225–230 (2010).
7. Pan, Y. D. et al. A large and persistent carbon sink in the world's forests. *Science* **333**, 988–993 (2011).
8. Le Quéré, C. et al. Global carbon budget 2016. *Earth Syst. Sci. Data* **8**, 605–649 (2016).
9. Boden, T. A., Marland, G. & Andres, R. J. Global, regional, and national fossil-fuel CO_2 emissions. In *Trends: A Compendium of Data on Global Change* (Carbon Dioxide Information Analysis Center, US Department of Energy, 2013).
10. Xu, L. et al. Temperature and vegetation seasonality diminishment over northern lands. *Nat. Clim. Change* **3**, 581–586 (2013).
11. Graven, H. D. et al. Enhanced seasonal exchange of CO_2 by northern ecosystems since 1960. *Science* **341**, 1085–1089 (2013).
12. Bond-Lamberty, B., Bailey, V. L., Chen, M., Gough, C. M. & Vargas, R. Globally rising soil heterotrophic respiration over recent decades. *Nature* **560**, 80–83 (2018).
13. Francey, R. J. & Frederiksen, J. S. The 2009–2010 step in atmospheric CO_2 interhemispheric difference. *Biogeosciences* **13**, 873–885 (2016).
14. Liu, Z. et al. Reduced carbon emission estimates from fossil fuel combustion and cement production in China. *Nature* **524**, 335–338 (2015).
15. Boggs, P. T. & Rogers, J. E. *Orthogonal Distance Regression*. Report No. NISTIR 89–4197 (National Institute of Standards and Technology, 1990).
16. Conway, T. J. & Tans, P. P. Development of the CO_2 latitude gradient in recent decades. *Glob. Biogeochem. Cycles* **13**, 821–826 (1999).
17. Le Quere, C. et al. Saturation of the Southern Ocean CO_2 sink due to recent climate change. *Science* **316**, 1735–1738 (2007).
18. Landschützer, P. et al. The reinvigoration of the Southern Ocean carbon sink. *Science* **349**, 1221–1224 (2015).
19. Brienen, R. J. W. et al. Long-term decline of the Amazon carbon sink. *Nature* **519**, 344–348 (2015).
20. Houghton, R. A. et al. Carbon emissions from land use and land-cover change. *Biogeosciences* **9**, 5125–5142 (2012).
21. Patra, P. K. et al. Transport mechanisms for synoptic, seasonal and interannual SF_6 variations and "age" of air in troposphere. *Atmos. Chem. Phys.* **9**, 1209–1225 (2009).
22. Hourdin, F. et al. The LMDZ4 general circulation model: climate performance and sensitivity to parametrized physics with emphasis on tropical convection. *Clim. Dyn.* **27**, 787–813 (2006).
23. Heimann, M. & Körner, S. *The Global Atmospheric Tracer Model TM3*. Technical Report No. 5 (Max Planck Institute for Biogeochemistry, 2003).
24. Prather, M. J., Holmes, C. D. & Hsu, J. Reactive greenhouse gas scenarios: Systematic exploration of uncertainties and the role of atmospheric chemistry. *Geophys. Res. Lett.* **39**, L09803 (2012).
25. Patra, P. K. et al. TransCom model simulations of CH_4 and related species: linking transport, surface flux and chemical loss with CH_4 variability in the troposphere and lower stratosphere. *Atmos. Chem. Phys.* **11**, 12813–12837 (2011).
26. Rödenbeck, C. et al. Global surface-ocean pCO_2 and sea–air CO_2 flux variability from an observation-driven ocean mixed-layer scheme. *Ocean Sci.* **9**, 193–216 (2013).
27. Landschützer, P., Gruber, N. & Bakker, D. C. E. *A 30 Years Observation-based Global Monthly Gridded Sea Surface pCO_2 Product from 1982 through 2011*. https://doi.org/10.3334/CDIAC/OTG.SPCO2_1982_2011_ETH_SOM-FFN (Carbon Dioxide Information Analysis Center, US Department of Energy, 2015).
28. Chevallier, F. et al. CO_2 surface fluxes at grid point scale estimated from a global 21 year reanalysis of atmospheric measurements. *J. Geophys. Res. D* **115**, D21307 (2010).
29. Rödenbeck, C., Houweling, S., Gloor, M. & Heimann, M. CO_2 flux history 1982–2001 inferred from atmospheric data using a global inversion of atmospheric transport. *Atmos. Chem. Phys. Discuss.* **3**, 2575–2659 (2003).
30. Denning, A. S., Fung, I. Y. & Randall, D. Latitudinal gradient of atmospheric CO_2 due to seasonal exchange with land biota. *Nature* **376**, 240–243 (1995).
31. Liu, X. et al. Enhanced nitrogen deposition over China. *Nature* **494**, 459–462 (2013).
32. Thomas, R. Q., Canham, C. D., Weathers, K. C. & Goodale, C. L. Increased tree carbon storage in response to nitrogen deposition in the US. *Nat. Geosci.* **3**, 13–17 (2010).
33. Che, H. Z. et al. Analysis of 40 years of solar radiation data from China, 1961–2000. *Geophys. Res. Lett.* **32**, L06803 (2005).

Acknowledgements We acknowledge the ocean modellers and the Dynamic Global Vegetation modellers (TRENDY-V4) who provided simulations for the global carbon budget assessment in ref. [8]. P.C. acknowledges support from the European Research Council Synergy project SyG-2013-610028 IMBALANCE-P and the ANR CLAND Convergence Institute. We thank the staff of the Scripps

Institution of Oceanography (SIO), the NOAA ESRL, the Japan Meteorological Agency (JMA) for the RYO station and the Izana Observatory/Meteorological State Agency of Spain (IO-MSAS) for the IZO station, who contributed to the collection of atmospheric data used in this study, in particular the long-term records from Mauna Loa and the South Pole.

Reviewer information *Nature* thanks Sander Houweling and the other anonymous reviewer(s) for their contribution to the peer review of this work.

Author contributions The study was conceived by P.C. and developed by P.C., J.T. and X.W. Simulations with the TM3 and LMDZ transport models were performed by C.R. and F.C. All other authors reviewed and provided input on the manuscript.

Competing interests The authors declare no competing interests.

Additional information
Extended data is available for this paper at https://doi.org/10.1038/s41586-019-1078-6.
Reprints and permissions information is available at http://www.nature.com/reprints.
Correspondence and requests for materials should be addressed to P.C.
Publisher's note: Springer Nature remains neutral with regard to jurisdictional claims in published maps and institutional affiliations.

METHODS

Two-box inversion. Because no global inversion of regional CO_2 fluxes using 3D transport fields covers the past 55 years, we constructed a two-box model to invert annual land CO_2 fluxes at the scale of the Northern and Southern hemispheres. Let C_N be the CO_2 mixing ratio in the Northern Hemisphere (represented by the Mauna Loa record), let C_S be the CO_2 mixing ratio in the Southern Hemisphere (represented by the South Pole record), and let the annual growth rates in the Northern and Southern hemispheres be $\dot{C}_N$ and $\dot{C}_S$, respectively. Given the inter-hemispheric mixing time τ, we have:

$$\alpha\dot{C}_S = F_N - O_N - L_N - \alpha\tau^{-1}(C_N - C_S) \quad (2)$$

$$\alpha\dot{C}_S = F_S - O_S - L_S + \alpha\tau^{-1}(C_N - C_S) \quad (3)$$

where $\dot{C}$ is the time derivative of deseasonalized CO_2 mixing ratios; F represents CO_2 emissions from the burning of fossil fuels, cement production and other industrial processes; O is the ocean sink; and L is the net land flux (including land use) counted positively if CO_2 is removed from the atmosphere; the subscripts N and S denote the Northern and Southern hemispheres, respectively. The conversion factor α between a hemispheric mixing ratio change of one p.p.m. per year and the corresponding flux in Pg C yr^{-1} in one hemisphere equals 1.06 Pg C per p.p.m.[24] Combining equations (2) and (3) gives:

$$IG = C_N - C_S = \frac{1}{2\alpha}\tau[(F_N - F_S) - (O_N - O_S) - (L_N - L_S) - \alpha(\dot{C}_N - \dot{C}_S)] \quad (4)$$

Equation (4) implies that the interhemispheric gradient is proportional to the flux difference between both hemispheres if the interhemispheric mixing rate is constant over time. $F_N - F_S$ is from CDIAC country data with the spatial patterns of EDGARv4.2, and $O_N - O_S$ is from an ocean model output driven by variable CO_2 and climate, available for the period 1959–2013[8]. These are the same ocean models as those used to infer the net land flux L in the global budget equation, so that our inference of L_N from equation (4) is consistent with that of L. We also tested two data-driven products for $O_N - O_S$ covering only the period starting from the early/mid-1980s[26,27] (see below). The change in interhemispheric gradient due to fossil-fuel and cement emissions alone in Fig. 1 was calculated by setting $O_N - O_S$ and $L_N - L_S$ to zero in equation (4) with an uncertainty of 10% for τ and 5% for F.

The grey-shaded 1-sigma error range of the L_N and L_S fluxes in the two-box inversion model (Fig. 4) is estimated using a Monte Carlo method with 5% uncertainty in F, an uncertainty of 0.18 Pg C yr^{-1} in the CO_2 growth rates at the South Pole (SPO) and at Mauna Loa (MLO), the standard deviation of all ocean models for $O_N - O_S$ and a 10% uncertainty for τ.

Long-term atmospheric CO_2 records. Long-term atmospheric CO_2 records used in this study are from continuous in-situ measurements at the MLO (1958–2013) and SPO (1958–2013) stations from the SIO network[34] downloaded as monthly averages from the SIO website (http://scrippsco2.ucsd.edu/data/atmospheric_co2/sampling_stations). For months with missing data, which represent only 15% of each record, CO_2 was gap-filled using standard curve-fitting algorithms[35] for atmospheric CO_2 data. In the early 1980s more atmospheric CO_2 stations became available, mainly from the NOAA ESRL network (Extended Data Table 1). From the GLOBALVIEWplus CO_2 data product giving monthly smoothed CO_2[36] (Cooperative Global Atmospheric Data Integration Project. 2013, thereafter continuously updated), we selected the stations with at least 8 years of data during 2000–2009 and at least 12 years of data during 1979–1999. We further selected only the records with more than 75% data coverage during any given month, and thus discarded stations with gaps where data from the Marine Boundary Layer composite curve was used to gap-fill CO_2 time series. This led us to retain ten stations from the NOAA ESRL, JMA and the IO-MSAS networks in the Northern Hemisphere covering the first and the second periods. Another two stations in the Northern Hemisphere were selected from the Scripps website (MLO, LJO (La Jolla, California, SIO)). For MLO—which was measured by both NOAA and Scripps—we used the longer Scripps record, leading to 11 long-term stations (Extended Data Table 1). The annual mean CO_2 mixing ratio was calculated from monthly smoothed data at each site to calculate the IG–F slopes. The uncertainty of IG–F slopes was estimated using a bootstrap method. We performed a linear regression analysis 1,000 times by randomly selecting a subset of 80% of samples from all pairs of IG and F during 1958–2013 accounting for uncertainties in IG and F. The standard deviation of those 1,000 slopes was used as the uncertainty of the slope. IG–F regression slopes are significant during both periods 1980–1999 and 2000–2009 for 7 out of 11 stations ($P < 0.01$). For four stations (LJO, ALT, KEY and MID) the IG–F slope correlation coefficient (r^2) is less than 0.3 during the first period. This leads to the selection of seven long-term Northern Hemisphere stations (BRW, STM, NWR, RYO, IZO, KUM and MLO) for IG–F slopes during both periods shown in Fig. 2. Slopes for each decade are shown in Extended Data Fig. 2.

Atmospheric 3D transport model of fossil-fuel CO_2. Atmospheric simulations of fossil-fuel CO_2 were performed with the global tracer transport model LMDZ[22] driven by the wind analyses from the European Centre for Medium-Range Weather Forecasts[37]. We use the model at the horizontal resolution of 3.75° longitude × 1.9° latitude with 39 vertical layers. This version has been the default transport model of the MACC inversion system since 2014, and earlier versions have participated in various intercomparisons within the TransCom project[25]. In the simulation of the fossil-fuel CO_2 tracer with LMDZ, emissions are from the CDIAC dataset[9] and have the spatial pattern of emissions of EDGARv4.2 (http://edgar.jrc.ec.europa.eu/), with yearly emissions in each country scaled to the CDIAC data each year. The global total emission from the CDIAC dataset includes bunker fuels, and thus is larger than the sum of emissions from all countries. In LMDZ, yearly bunker fuel emissions are distributed using the EDGARv4.2 spatial patterns. No intra-annual variation of fossil-fuel CO_2 emissions was assumed if country-specific information was absent, although the seasonality of emissions may be regionally significant[38].

Similar simulations were performed using the TM3 transport model[23] driven either by the NCEP[39] or by the ERA-Interim[37] reanalysis transport fields. The model was run at the horizontal resolution of 5° longitude × ~4° latitude, with 19 vertical layers (NCEP) or 26 vertical layers (ERA-Interim). Fossil-fuel and cement emissions were taken from EDGAR 4.2 (with FT2010 for 2009 and 2010, extrapolation based on BP global totals for 2011 and 2012, and an increase of 2% per year afterwards). All categories provided by EDGAR 4.2 were added, except for biomass burning. The yearly emission maps were smoothly interpolated in time.

MACC inversion. We used the CO_2 inversion product[28] v14r2 of the Monitoring Atmospheric Composition and Climate service (MACC, https://atmosphere.copernicus.eu/). Since 2010, this product has been released every year, based on the assimilation of surface-air-sample mole fraction measurements within the LMDZ transport model[22]. The list of the >130 assimilated sites is given in the supplementary material of ref. [40]. This inversion relies on a variational formulation that estimates eight-day grid-cell (3.75° longitude × 1.9° latitude) daytime/night time CO_2 fluxes and the grid cell total columns of CO_2 at the initial time step of the inversion window. It enables several decades (here the 1979–2014 period) to be processed in a single assimilation window, therefore ensuring the physical and statistical consistency of the inversion over the full measurement period. The previous ocean flux is from the climatology[41] based on Δp_{CO_2} observations, with no trend and no interannual variability. The previous land flux is based on a climatology from a simulation of the ORCHIDEE land surface model with no interannual variability, fire emissions have a priori values with interannual variability from GFED4[42], and annual mean net ecosystem exchange over grid-cells affected by fires is forced to zero, implying full regrowth in the same year as the fires.

JENA inversion. The Jena CarboScope atmospheric CO_2 inversion (version s81_v3.7) uses a set of 14 measurement stations selected to completely cover the 1981–2014 estimation period of this run. It uses individual measurements from various sampling networks, without smoothing or gap filling. Fluxes are estimated at the grid-scale resolution (~4° latitude × 5° longitude) to reduce aggregation errors. However, to counteract that the estimation would be underdetermined, spatial and temporal a priori correlations are imposed, smoothing the estimated flux field on scales smaller than about 1 week and about 1,600 km (land, in longitude direction), 800 km (land, latitude), 1,900 km (ocean, longitude) or 950 km (ocean, latitude), respectively. Land-flux adjustments are spatially weighted with a productivity proxy (long-term mean net primary productivity from the LPJ model). Previous fluxes comprise anthropogenic CO_2 emissions (from EDGAR 4.2), a constant spatial flux pattern on land (time-mean net ecosystem exchange from the LPJ model), and a mean seasonal cycle on the ocean (from the ocean-interior inversion in ref. [43], with seasonality from ref. [44]). The JENA inversion uses the TM3 global atmospheric transport model driven by meteorology from the ERA-Interim reanalysis. The optimization is performed by a single cost-function minimization for the entire estimation period plus spin-up and spin-down periods[45]. See http://www.bgc-jena.mpg.de/CarboScope/ for further information and to download the dataset.

Northern land carbon sink from land carbon models. We used the monthly land CO_2 fluxes calculated by process-based land models over the period 1959–2013. The nine land carbon cycle models are from the TRENDYv4 project[5], used for the independent assessment of the land sink variability in ref. [11]. Each model, the common initialization and transient twentieth-century simulation protocols are described in ref. [5]. The majority of the land models produce a sink because they calculate a net imbalance between increasing photosynthesis (gross primary productivity) and the lagged response of total ecosystem respiration in response to increasing CO_2 levels, variable climate and land-cover change (S3 simulations). Only four land models include fire emissions, which are part of the net land flux. One model out of ten in the original TRENDY v4 ensemble was excluded because it gave a strong global land source (LPX). The models used are CLM4-5, JSBACH, JULES, LPJG, OCN, VEGAS, VISIT, ISAM and ORCHIDEE (Extended Data Fig. 7). Only three models account for carbon–nitrogen biogeochemical

interactions and atmospheric nitrogen deposition (CLM4-5, OCN and ISAM), the latter occurring mainly over northern lands and being an additional driving force of the northern carbon sink.

Air–sea carbon flux interhemispheric difference from ocean biogeochemical models and from data-driven models. Ocean biogeochemical models used for the period 1959–2013 are NEMO-PlankTOM5, NEMO-PISCES (IPSL), MPIOM-HAMOCC, MICOM-HAMOCC (NorESM-OC), NEMO-PISCES (CNRM), CSIRO and CCSM-BEC; these models represent the physical, chemical and biological processes that influence the surface ocean concentration of CO_2 and thus the air–sea CO_2 flux. The ocean CO_2 sink for each model is normalized to observations, by dividing the annual model values by their observed average over 1990–1999, and multiplying this by the observation-based estimate of 2.2 Pg C yr^{-1} as in ref. [8]. To model the global distribution of air–sea CO_2 fluxes—which are obtained by interpolation of p_{CO_2} data from the SOCAT database—over time, and to model gas exchange formulations during the past three decades, we used two data-driven models[26,27], covering 1985–2012 (ref. [26]) and 1982–2011 (ref. [27]).

Data availability

The decadal CO_2 flux data that support the findings of this study are available in the Extended Data tables. Annual flux data from the two-box model and other models are available at http://dods.lsce.ipsl.fr/invsat/PC/. Atmospheric CO_2 data are available from the Scripps Institution for Oceanography (SIO) website http://scrippsco2.ucsd.edu/data/atmospheric_co2/sampling_stations for MLO, LJO and SPO stations and from the ESRL GLOBALVIEW-plus CO_2 open access dataset for other stations (https://www.esrl.noaa.gov/gmd/ccgg/obspack/our_products.php).

34. Keeling, C. D., Piper, S. C. et al. *Exchanges of Atmospheric CO_2 and $^{13}CO_2$ with the Terrestrial Biosphere and Oceans from 1978 to 2000. I Global Aspects* (University of California, San Diego, Scripps Institution of Oceanography, 2001).
35. Thoning, K. W., Tans, P. P. & Komhyr, W. D. Atmospheric carbon dioxide at Mauna Loa Observatory: 2. Analysis of the NOAA GMCC data, 1974–1985. *J. Geophys. Res. D* **94**, 8549–8565 (1989).
36. Masarie, K. A., Peters, W., Jacobson, A. R. & Tans, P. P. ObsPack: a framework for the preparation, delivery, and attribution of atmospheric greenhouse gas measurements. *Earth Syst. Sci. Data* **6**, 375–384 (2014).
37. Dee, D. P. et al. The ERA-Interim reanalysis: configuration and performance of the data assimilation system. *Q. J. R. Meteorol. Soc.* **137**, 553–597 (2011).
38. Blasing, T. J., Broniak, C. T. & Marland, G. The annual cycle of fossil-fuel carbon dioxide emissions in the United States. *Tellus B* **57**, 107–115 (2005).
39. Kalnay, E. et al. The NCEP/NCAR 40-year reanalysis project. *Bull. Am. Meteorol. Soc.* **77**, 437–472 (1996).
40. Chevallier, F. On the statistical optimality of CO_2 atmospheric inversions assimilating CO_2 column retrievals. *Atmos. Chem. Phys.* **15**, 11133–11145 (2015).
41. Takahashi, T. et al. Climatological mean and decadal change in surface ocean pCO_2, and net sea-air CO_2 flux over the global oceans. *Deep Sea Res. II* **56**, 554–577 (2009).
42. van der Werf, G. R. et al. Global fire emissions estimates during 1997–2016. *Earth Syst. Sci. Data* **9**, 697–720 (2017).
43. Mikaloff Fletcher, S. E. et al. Inverse estimates of anthropogenic CO_2 uptake, transport, and storage by the ocean. *Glob. Biogeochem. Cycles* **20**, https://doi.org/10.1029/2005GB002530 (2006).
44. Takahashi, T. et al. Global sea–air CO_2 flux based on climatological surface ocean pCO_2, and seasonal biological and temperature effects. *Deep Sea Res. II* **49**, 1601–1622 (2002).
45. Rödenbeck, C. *Estimating CO_2 Sources and Sinks from Atmospheric Mixing Ratio Measurements using a Global Inversion of Atmospheric Transport*. Technical Report No. 6 (Max-Planck-Institut für Biogeochemie, 2005).

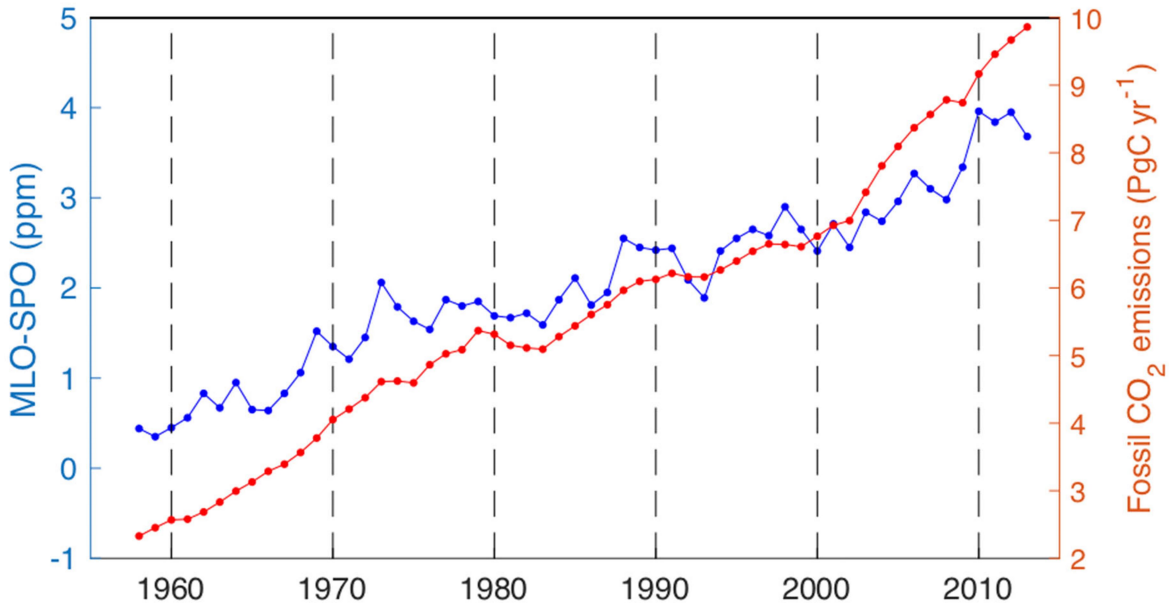

Extended Data Fig. 1 | Evolution of the interhemispheric CO_2 gradient and of CO_2 emissions from fossil fuels and cement. The interhemispheric CO_2 gradient, defined by the difference in observed mixing ratios between the MLO and SPO monitoring stations (blue), and the global CO_2 emissions from fossil-fuel and cement obtained from CDIAC (red), both shown from 1958 to 2013.

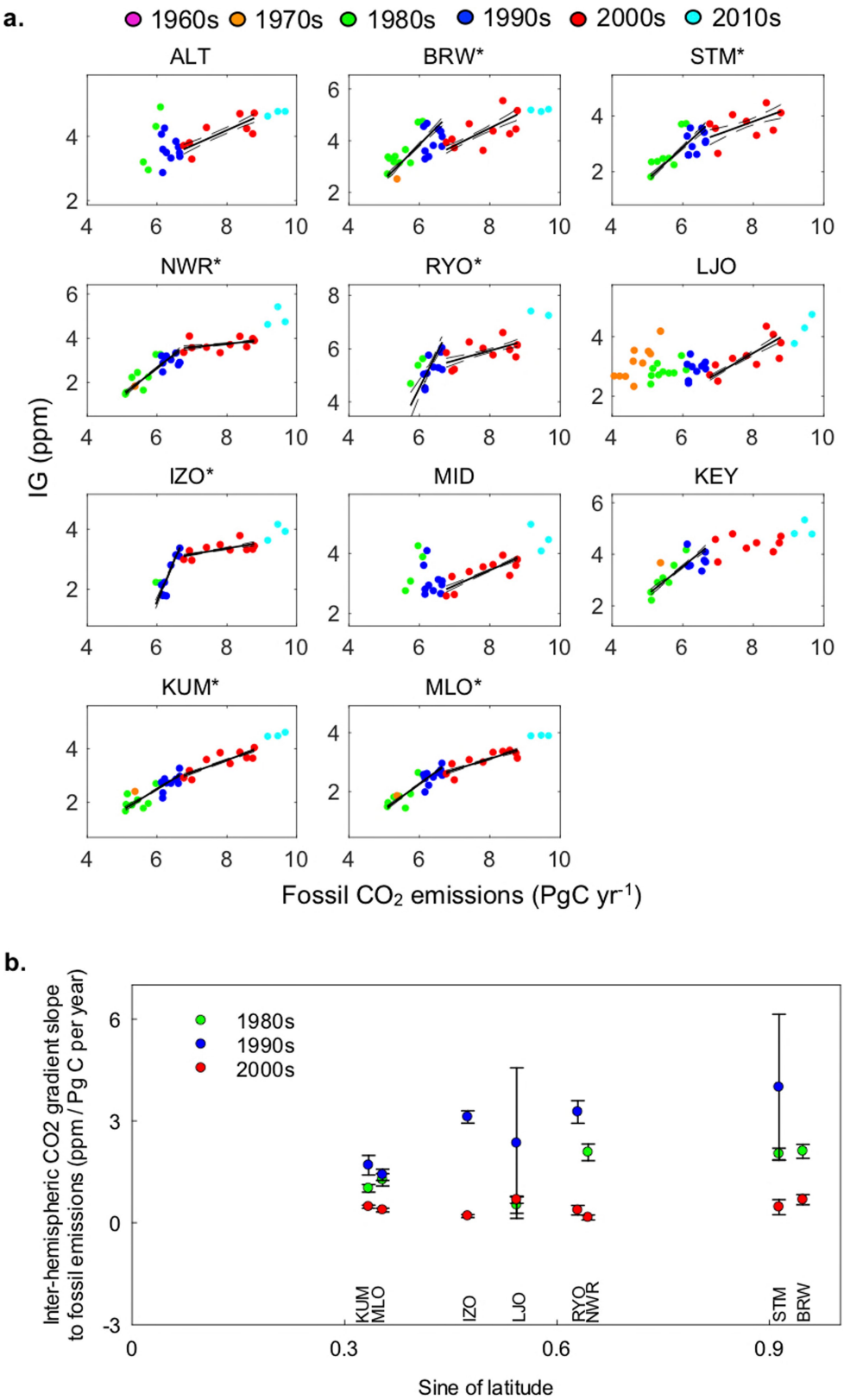

Extended Data Fig. 2 | Interhemispheric CO_2 gradient plotted against fossil-fuel CO_2 emissions for each decade from the 1960s to the 2010s, and IG–F slopes in the 1980s, 1990s and 2000s. a, Scatter plots of the interhemispheric gradient plotted against emissions from fossil fuels and cement, obtained from CDIAC, for different Northern Hemisphere long-term monitoring stations with sufficient data coverage (see Methods). The SPO station is always taken as the reference from which to calculate the interhemispheric gradient from each station. A station is marked by an asterisk if the correlation coefficient (r^2) between interhemispheric gradient and emissions is greater than 0.3 during both period 1 (first available year to 1999) and period 2 (2000 to 2009). **b**, Decadal linear regression IG–F slopes at the long-term monitoring stations for which the correlation coefficient between interhemispheric gradient and emissions is greater than 0.3 during any of the past three decades. The SPO station is taken as the reference from which to calculate the interhemispheric gradient for each station. The slope was calculated at each site and error bars represent the orthogonal data regression slope uncertainties.

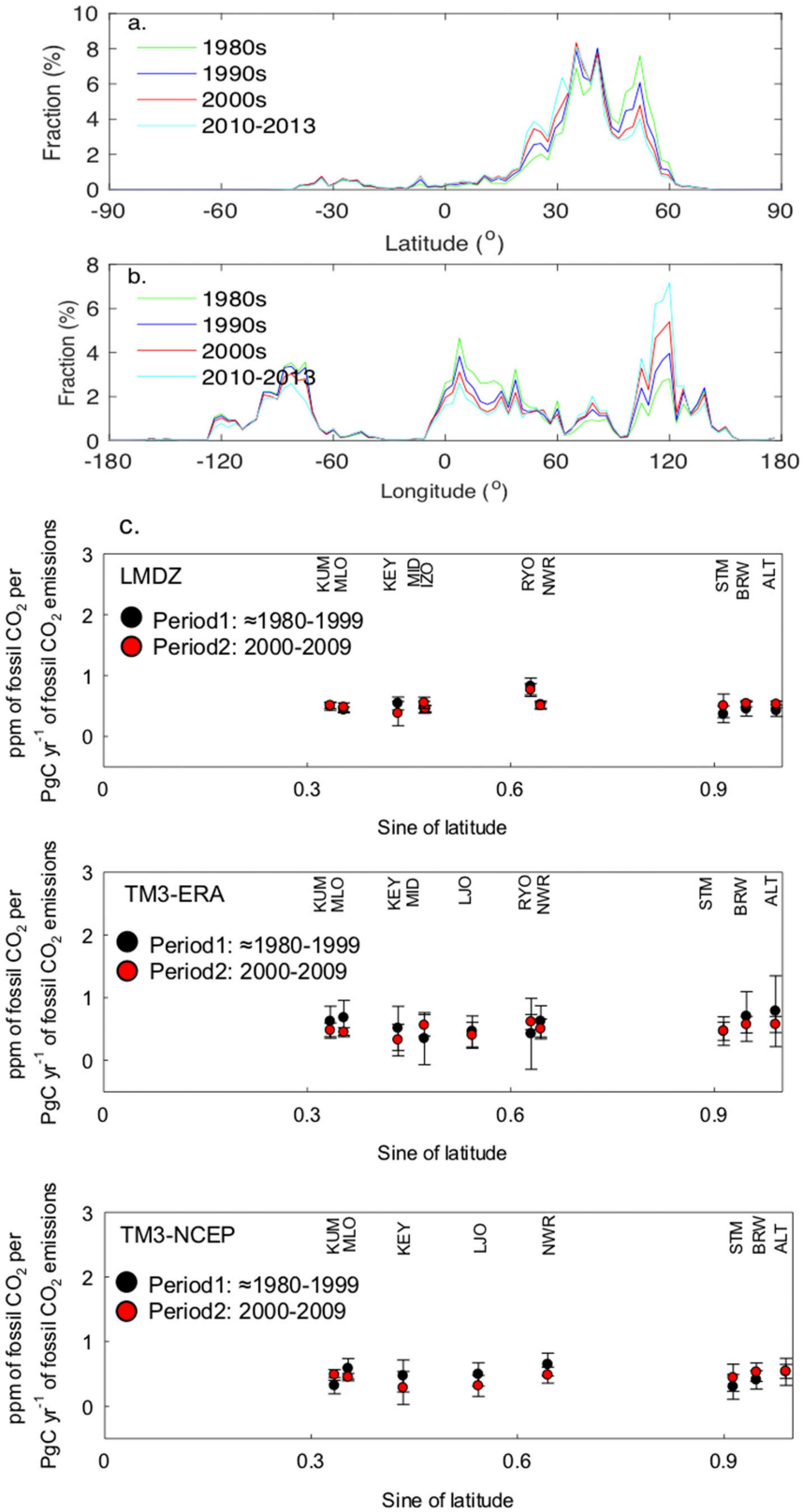

Extended Data Fig. 3 | The proportion of fossil-fuel emissions by latitude and longitude for each decade from the 1980s, and simulated IG–F slopes from ~1980–1999 and in the 2000s with three different atmospheric transport models. a, **b**, Fraction of global fossil-fuel CO_2 emissions in each latitude band (**a**) and in each longitude band (**b**) during 1980–2013. **c**, Slope of orthogonal least square linear regressions between modelled interhemispheric gradient for a simulated fossil-fuel CO_2 tracer (see Methods) and fossil CO_2 emissions. Three global 3D transport models were used with interannual winds to obtain these results (Methods), namely LMDZ with ERA-Interim ECMWF winds (top), TM3 with ERA-Interim ECMWF winds (middle) and TM3 with NCEP winds (bottom). LMDZ and TM3 were prescribed time-varying maps of fossil-fuel and cement emissions. The modelled distribution of the fossil-fuel CO_2 tracer in the atmosphere was sampled at the location of each long-term station. The slopes are shown for two periods: from around 1980–1999 (the first year of observations at each site is around 1980) and 2000–2009. The modelled fossil-fuel CO_2 tracer at SPO is taken as a reference from which to calculate the interhemispheric gradient at all sites.

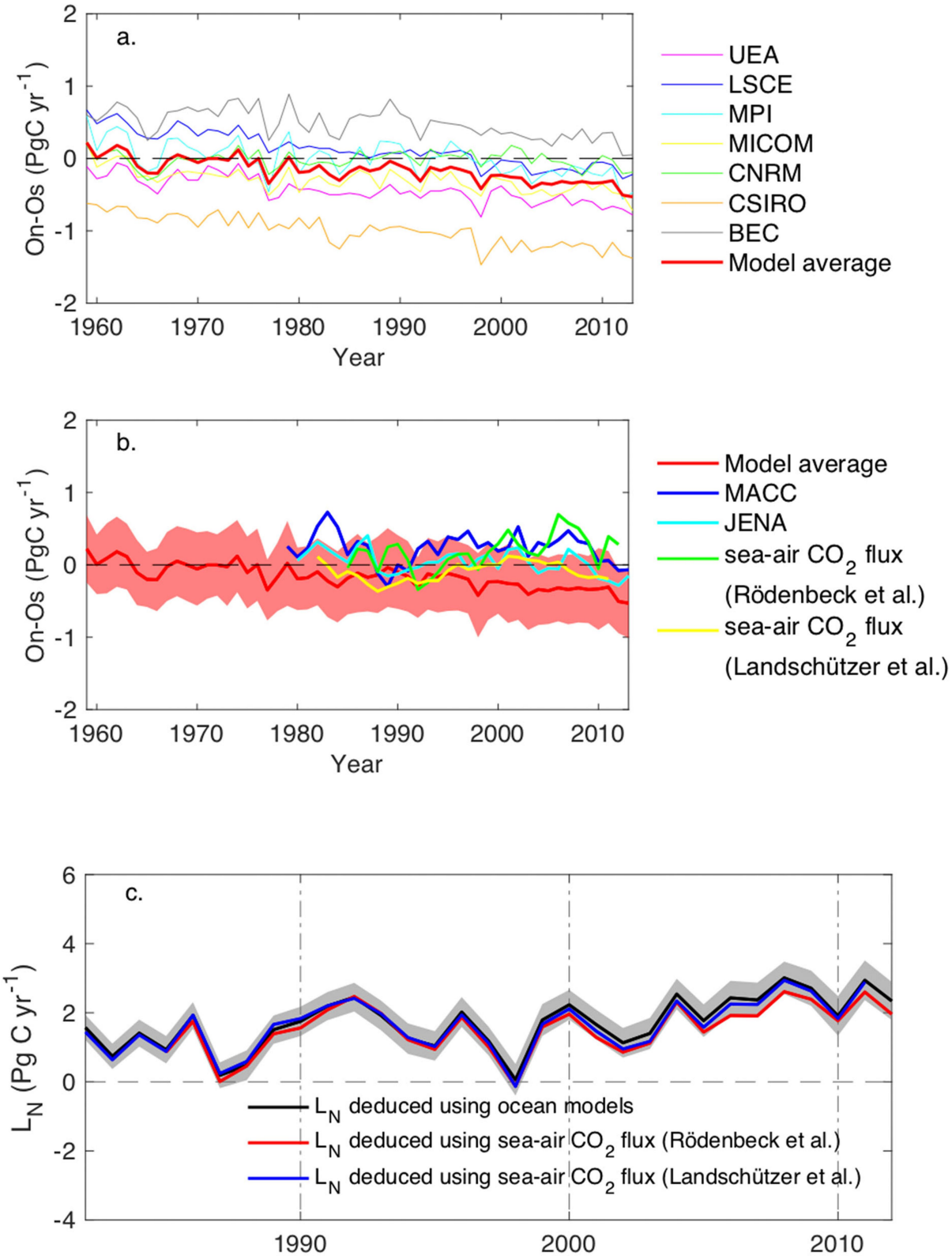

Extended Data Fig. 4 | Ocean flux differences between the Northern and Southern hemispheres from ocean biogeochemical models, data-driven models and inversions. a, Interhemispheric difference in ocean fluxes ($O_N - O_S$) between 1959 and 2013, obtained from the seven ocean models used in ref. [17]. **b**, Estimates of ($O_N - O_S$) from MACC and JENA inversion results over the period they cover, and from the two ocean data-driven models described in the Methods[26,27]. **c**, L_N inferred from the two-box inversion, with ($O_N - O_S$) being the mean value from seven ocean models (black line) and from each of the two data-driven models (red and blue lines)[26,27].

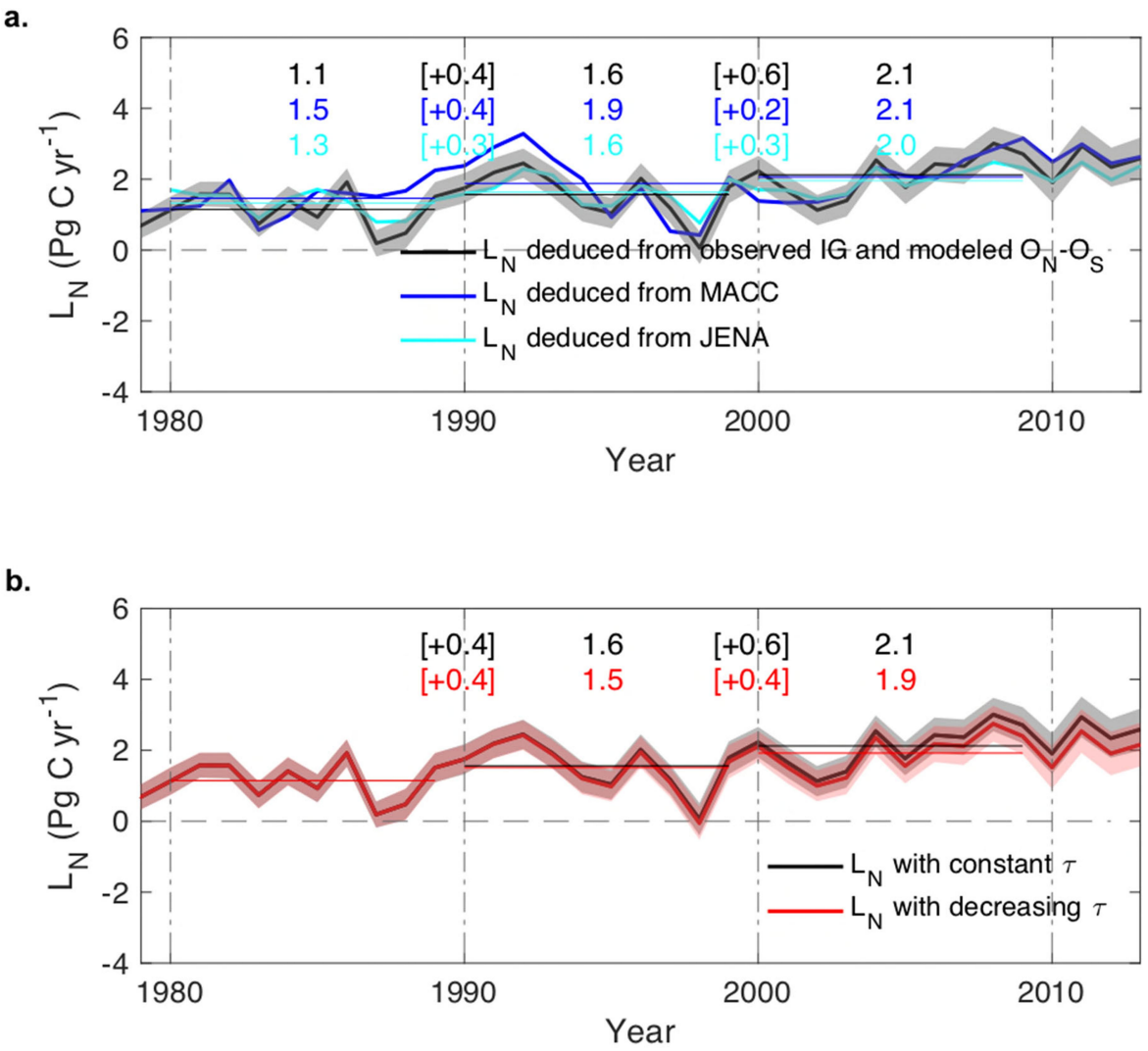

Extended Data Fig. 5 | Northern land sink from inversions, with decadal mean values shown, and the sensitivity of the northern land sink to interhemispheric mixing time. a, Values of the northern land sink obtained from two-box inversion (black, with 1-sigma uncertainty in grey) and from MACC (dark blue) and JENA (light blue) 3D inversions. In the 3D inversions, L_N is calculated by summing the flux of land grid cells north of the Equator. Numbers indicate decadal mean values, and the numbers in brackets denote the change in L_N from one decade to the next. **b**, Comparison of L_N inferred by the two-box inversion in the control case (black) in which the interhemispheric mixing time is set constant at 1.4 years, and in a scenario (red) in which it is inferred from SF_6 measurements to have decreased linearly by 0.57% per year from 1990 to 2013, corresponding to the fraction of the decrease observed in ref. [21] that was not explained by a southward shift in geographic distribution of SF_6 emissions.

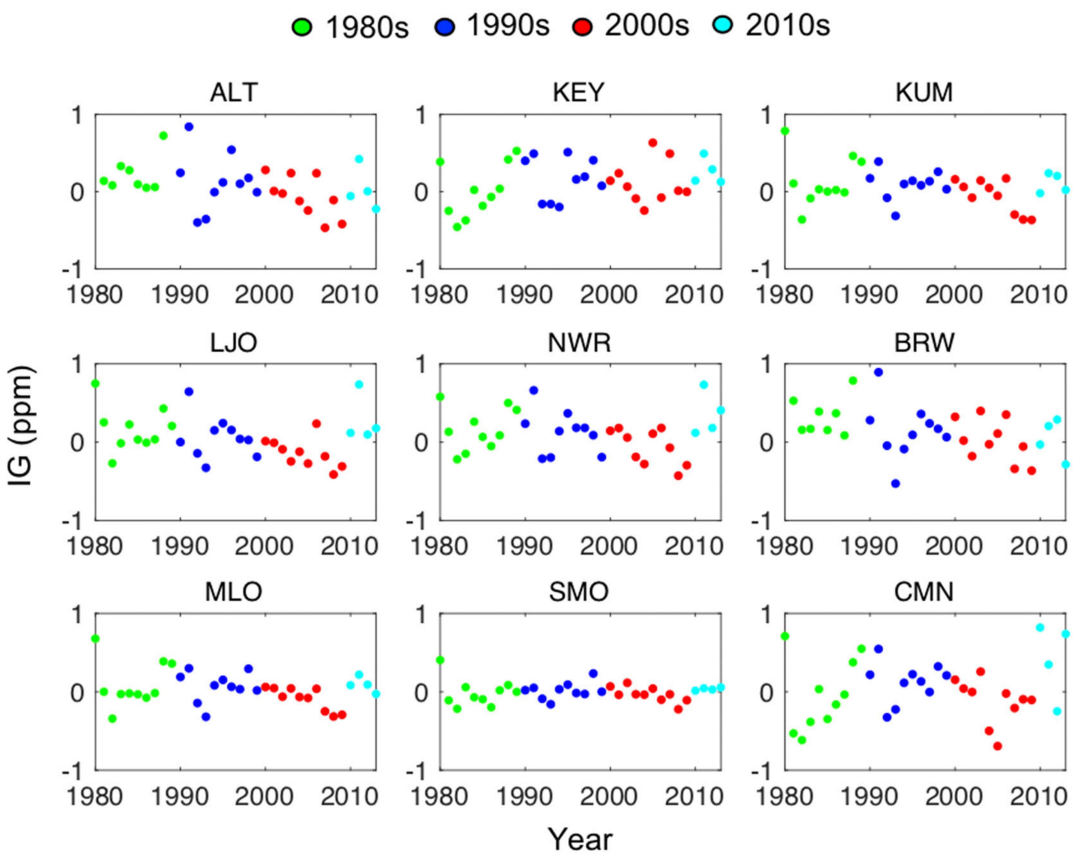

Extended Data Fig. 6 | Trend in 'rectifier interhemispheric CO_2 gradient' simulated with TM3 related to the trend of atmospheric transport convoluted by trends in the seasonal amplitude and phase of land–atmosphere fluxes. Scatter diagrams of simulated change in interhemispheric gradient with TM3 and ERA-interim wind fields (see Methods) related to the trend of atmospheric transport convoluted by trends in the seasonal amplitude and phase of land–atmosphere fluxes, called 'trend in rectifier'. The results are obtained by applying TM3 to variable maps of seasonal land fluxes created by subtracting the mean seasonal cycle and the long-term mean from the inverted land fluxes (at every grid cell). Then, the simulated CO_2 field was sampled at the same location as each long-term station, and the difference from the value obtained at the SPO station is plotted as interhemispheric gradient due to 'trend in rectifier'. The absence of any trend in interhemispheric gradient from 'trend in rectifier'-related mechanisms suggests that this process does not explain any trend in the observed interhemispheric gradient that would be aliased as trends in L_N in the two-box inversion.

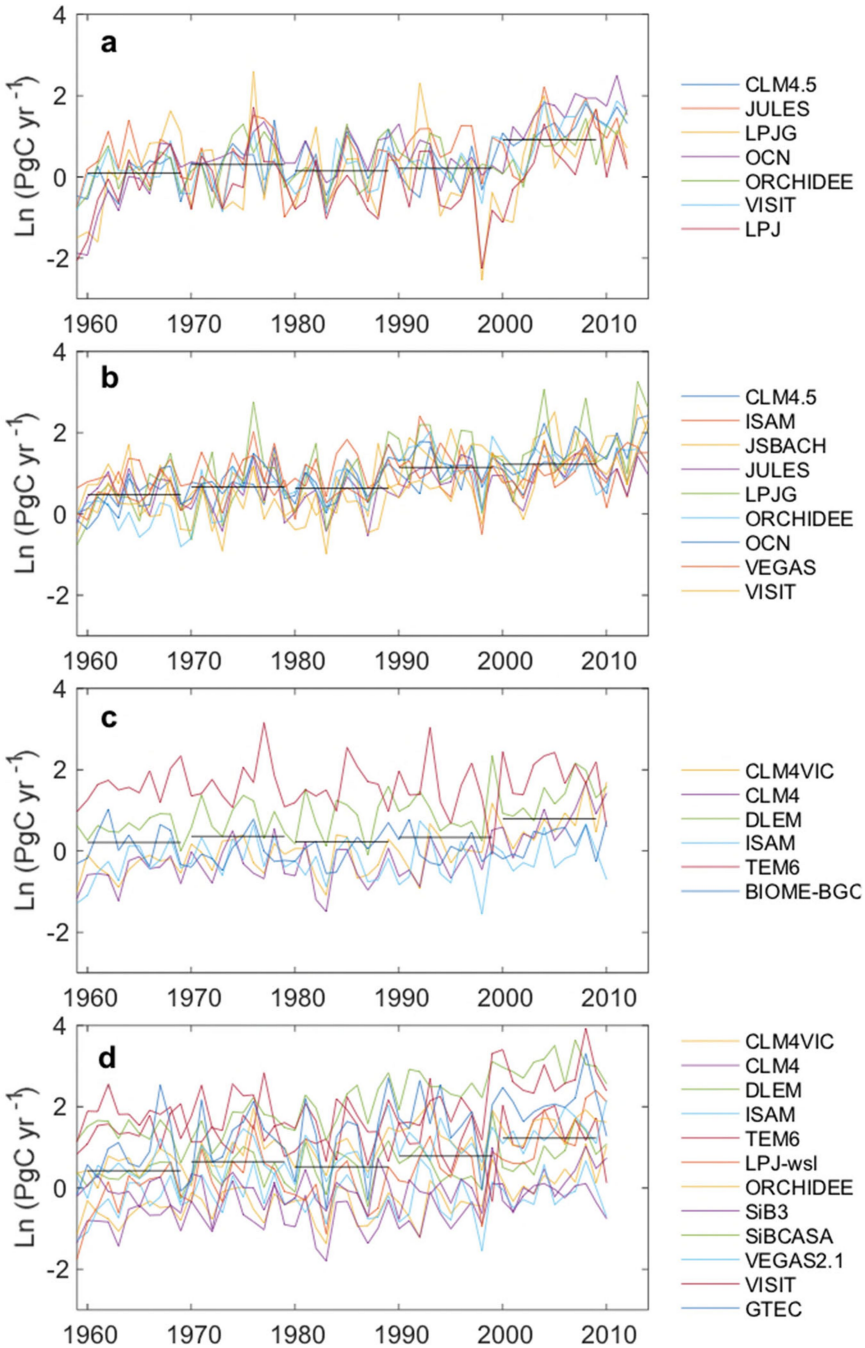

Extended Data Fig. 7 | Northern land sink simulated by different land carbon-cycle models. a, TRENDY V2 ensemble (1959–2012), **b**, TRENDY V4 ensemble used in this study (1959–2014), **c**, MsTMIP ensemble with models considering nitrogen deposition change (1959–2010), **d**, MsTMIP ensemble with models not considering nitrogen deposition change (1959–2010). MsTMIP models with CO_2 sources in the Northern Hemisphere and/or global land sink that lie outside the observed range from the global CO_2 budget of ref. [17] were not used.

Extended Data Table 1 | Atmospheric stations with long-term CO_2 records since the early 1980s

Site	Lat	Lon	Type	Network	Start year	End year	Slope	Std.
BRW	71.3	-156.6	continuous	NOAA ESRL	1979	2012	0.49	0.04
STM	66	2	flask	NOAA ESRL	1982	2008	0.57	0.05
NWR	40.1	-105.6	flask	NOAA ESRL	1979	2012	0.66	0.04
RYO	39	141.8	continuous	JMA	1987	2012	0.58	0.05
IZO	28.3	-16.5	continuous	IO-MSAS	1988	2012	0.51	0.04
KUM	19.5	-154.8	flask	NOAA ESRL	1979	2012	0.59	0.02
MLO	19.5	-155.6	continuous	Scripps	1958	2013	0.49	0.01
MLO	19.5	-155.6	continuous	NOAA ESRL	1979	2012	0.49	0.02
ALT	82.5	-62.5	flask	NOAA ESRL	1986	2012	0.36	0.04
LJO	32.9	-117.3	flask	Scripps	1969	2012	0.22	0.03
MID	28.2	-177.4	flask	NOAA ESRL	1986	2012	0.36	0.05
KEY	25.7	-80.2	flask	NOAA ESRL	1979	2012	0.49	0.04

The seven stations used in the analysis are listed first. For the four following stations shown in red, the regression slope of the interhemispheric gradient plotted against fossil-fuel emissions (IG–F) in p.p.m. per Pg C per year had a correlation coefficient of less than 0.3 during either period 1 (1980–1989) or period 2 (1990–1999). Values from the MLO station that were obtained by NOAA ESRL (in blue) were not used; instead, the longer Scripps record was used.

Extended Data Table 2 | Linear regression slopes of the interhemispheric CO_2 gradient against fossil-fuel emissions at long-term atmospheric stations

Site	Latitude	Slope from ODR (1σ) Period 1 1980s and 1990s	Slope from ODR (1σ) Period 2 2000s	Correlation coefficient (R) Period 1 1980s and 1990s	Correlation coefficient (R) Period 2 2000s
ALT	82.5	N/A	0.48 (0.10)	0.04	0.76
BRW	71.3	1.37 (0.20)	0.68 (0.15)	0.66	0.60
STM	66	1.15 (0.15)	0.46 (0.25)	0.67	0.43
NWR	40.1	1.24 (0.10)	0.15 (0.07)	0.81	0.39
RYO	39	2.65 (0.40)	0.37 (0.11)	0.54	0.51
LJO	32.9	N/A	0.67 (0.11)	-0.03	0.75
IZO	28.3	2.75 (0.32)	0.20 (0.04)	0.86	0.62
MID	28.2	N/A	0.51 (0.09)	-0.21	0.78
KEY	25.7	1.09 (0.11)	N/A	0.72	0.21
KUM	19.5	0.81 (0.07)	0.47 (0.06)	0.82	0.83
MLO	19.5	0.87 (0.06)	0.37 (0.06)	0.87	0.82

Slopes at the long-term stations are given for period 1 (1980–1999) and period 2 (2000–2009). All slope values are in p.p.m. per Pg C per year. Uncertainties of the slopes, in parentheses, are 1-sigma. Red numbers are stations with correlation coefficient of less than 0.3, for which the slope was not calculated (N/A).

Extended Data Table 3 | Summary of estimates of the northern land sink

a.

		1960s	1970s	1980s	1990s	2000s	2010-2013	1960-2013
Fossil emissions	F	3.1 ± 0.2	4.7 ± 0.3	5.5 ± 0.3	6.4 ± 0.33	7.9 ± 0.4	9.5 ± 0.5	5.8 ± 0.3
Net land sink	L	0.2 ± 0.6	0.4 ± 0.6	0.2 ± 0.6	1.1 ± 0.6	1.5 ± 0.7	2.0 ± 0.7	0.8 ± 0.6
Northern land sink	L_N	0.9± 0.3	1.1 ± 0.4	1.1 ± 0.4	1.6 ± 0.4	2.1 ± 0.5	2.4 ± 0.6	1.4 ± 0.4
	$L_{N\,MACC}$			1.5 ± 0.3	1.9 ± 0.3	2.1 ± 0.3	2.6 ± 0.3	
	$L_{N\,JENA}$			1.3	1.6	2.0	2.2	
	$L_{N\,mod}$	0.5±0.3	0.7±0.3	0.6±0.3	1.1±0.3	1.2±0.2	1.4±0.4	0.9 ± 0.2

b.

Northern land sink in Land carbon models (TRENDY v4)	**1960s**	**1970s**	**1980s**	**1990s**	**2000s**	**2010-2013**
JULES	0,6	0,5	0,3	0,9	1,0	1,0
JSBACH	0,7	0,6	0,5	1,5	1,5	1,8
VEGAS	0,5	0,8	0,7	1,2	1,0	1,4
ORCHIDEE	-0,1	0,5	0,8	1,3	1,2	1,4
LPJ GUESS	0,5	0,8	0,8	1,4	1,6	1,9
VISIT	0,2	0,1	0,0	0,7	1,0	1,2
ISAM ^{N}	0.9	1.1	1.1	1.0	1.1	0.8
OCN ^{N}	0,4	0,8	0,7	1,3	1,5	1,8
CLM4.5 ^{N}	0,4	0,7	0,7	1,0	1,1	1,1
Mean of models (± std.)	0.5±0.3	0.7±0.3	0.6±0.3	1.1±0.3	1.2±0.2	1.4±0.4

a, Decadal mean and long-term mean fossil-fuel emissions, net land sink and northern land sink over the past five decades. **b**, Decadal mean in northern land sink from TRENDY V4 land carbon-cycle models. Models with carbon–nitrogen interactions are denoted with superscript N.